Scaling Effect on Prediction of Cavitation Inception in a Line Vortex Flow

Chao-Tsung Hsiao
Georges L. Chahine
Dynaflow, Inc.,
10621-J Iron Bridge Road,
Jessup, MD 20794
e-mail: info@dynaflow-inc.com

Han-Lieh Liu
U.S. Patent and Trademark Office,
Crystal Plaza 3, Room 2C02
Washington, DC 20231

The current study considers the prediction of tip vortex cavitation inception at a fundamental physics based level. Starting form the observation that cavitation inception detection is based on the "monitoring" of the interaction between bubble nuclei and the flow field, the bubble dynamics is investigated in detail. A spherical model coupled with a bubble motion equation is used to study numerically the dynamics of a nucleus in an imposed flow field. The code provides bubble size and position versus time as well as the resulting pressure at any selected monitoring position. This model is used to conduct a parametric study. Bubble size and emitted sound versus time are presented for various nuclei sizes and flow field scales in the case of an ideal Rankine vortex to which a longitudinal viscous core size diffusion model is imposed. Based on the results, one can deduce cavitation inception with the help of either an "optical inception criterion" (maximum bubble size larger than a given value) or an "acoustical inception criterion" (maximum detected noise higher than a given background value). We use here such criteria and conclude that scaling effects can be inherent to the way in which these criteria are exercised if the bubble dynamics knowledge is not taken into account.
[DOI: 10.1115/1.1521956]

1 Introduction

It is common to predict tip vortex cavitation inception in a small-scale laboratory setting. The challenge is then to find the correct scaling laws to extrapolate the results to the full scale. While the present knowledge of the scaling laws enables engineers to proceed properly in many cases, there are conditions where classical scaling as defined below needs to be reconsidered and corrected. This paper aims at contributing to the knowledge needed to describe such a more general scaling.

In practice, engineering prediction of cavitation inception is made by equating the cavitation inception number to the negative of the minimum pressure coefficient neglecting real flow effects such as nuclei presence and dynamics, and bubble/flow interactions and unsteadiness, These ignored effects sometimes lead to significant discrepancies between model and full-scale tests and to "*scale effects.*"

The nondimensional cavitation number, σ, used to characterize overall cavitation effects is defined as

$$\sigma=\frac{p_\infty-p_v}{1/2\rho V_\infty^2}, \tag{1}$$

where p_∞ and V_∞ are the characteristic pressure and velocity (usually at freestream), ρ is the liquid density, and p_v is the liquid vapor pressure. Following McCormick [1], several experimental studies have established the following scaling law to predict steady tip vortex cavitation inception:

$$\sigma_i=KC_l^2R_e^\alpha, \quad \text{with} \quad R_e=\frac{V_\infty C_0}{v}. \tag{2}$$

K is a proportionality constant, which depends on the foil geometry and the flow incidence, C_l is the foil lift coefficient, and R_e is the flow Reynolds number based on the hydrofoil chord length, C_0. Equation (2) correlates the cavitation inception number, σ_i, to the boundary layer growth on the foil. Different values of α have been proposed in previous studies. For example, McCormick [1] found $\alpha=0.35$ while Fruman et al. [2] and Arndt and Dugue [3] used $\alpha=0.40$. Farrell and Billet [4] proposed a correlation model for leakage vortex cavitation inception with $\alpha=2/7$. Arndt and Keller [5] introduced a correction term to Eq. (2) based on the "tensile strength" of the liquid to account for the presence of nuclei and the onset of cavitation in "*weak*" and "*strong*" water. However, they did not account directly for the effect of nuclei dynamics per se.

Direct experimental observation of bubble capture by the tip vortex is difficult due to the small size of the nuclei and the high local velocities. Numerical studies, therefore, have been used primarily to study these effects. The complexity of the cavitation inception process, however, has led various numerical studies to neglect one or more of the factors, and therefore to only investigate the influence of a limited set of parameters. Most models accept that tip vortex cavitation inception is due to traveling bubbles, and use a spherical bubble dynamics model coupled with a motion equation to predict cavitation inception. Latorre [6] and Ligneul and Latorre [7] applied this approach to deduce noise emission from cavitation in a Rankine line vortex. Hsiao and Pauley [8] further applied this approach to study tip vortex cavitation inception with the tip vortex flow field computed by Reynolds-averaged Navier-Stokes equations.

The current study makes a concerted effort to investigate the importance of the nuclei size on tip vortex cavitation inception. The tip vortex flow of a three-dimensional foil is idealized as a Rankine vortex. Empirical equations are used to estimate the vortex strength and core size for three different foil sizes. A modified spherical model is then implemented and used to predict inception. Both an "*acoustic*" criterion (emitted sound level higher than a threshold value) and an "*optical*" criterion (bubble size larger than a threshold value) are considered for "calling" the cavitation inception. The characteristics of the acoustic pressure signals due to the bubble dynamics are also computed and analyzed.

2 Numerical Method

2.1 Rankine Vortex Model. We consider the tip vortex generated by a finite-span hydrofoil and consider three different

Contributed by the Fluids Engineering Division for publication in the JOURNAL OF FLUIDS ENGINEERING. Manuscript received by the Fluids Engineering Division May 18, 2001; revised manuscript received July 1, 2002. Associate Editor: E. Graf.

Table 1 Conditions of the three scale tests considered

	Small Scale	Medium Scale	Large Scale
λ	1/48	1/4	1
C_0 (m)	0.0508	0.6096	2.4384
V_∞ (m/sec)	10	12.5	15
Γ (m²/sec)	0.12767	1.91511	9.19255
R_e	5.08×10^5	7.62×10^6	3.66×10^7
a_c (m)	0.001358	0.009486	0.02770
$C_{p\ \min}$	−4.474	−13.215	−24.797

sizes of this foil, small (laboratory 1/48 scale), medium (1/4 scale), and large (full scale). These hydrofoils are geometrically similar and are operated at the same angle of attack. The tip vortex flow field is represented by a Rankine line vortex for which the rotation velocity, u_θ, and pressure, p_ω, of the vortical flow are given by

$$u_\theta(r)=\left\{\frac{\Gamma}{2\pi a_c^2}r,\quad r\leq a_c;\quad \frac{\Gamma}{2\pi r},\quad r>a_c\right\},\tag{3}$$

$$p_\omega(r)=\left\{\begin{array}{ll} p_\infty-\dfrac{\rho\Gamma^2}{4\pi^2 a_c^2}+\dfrac{\rho\Gamma^2 r^2}{8\pi^2 a_c^4}, & r\leq a_c \\ p_\infty-\dfrac{\rho\Gamma^2}{8\pi^2 r^2}, & r>a_c\end{array}\right\}.\tag{4}$$

The circulation strength, Γ, is obtained based on the equation described in Abbott and Doenhoff [9]:

$$\Gamma=\frac{1}{2}\left(A_0+\frac{1}{2}A_1\right)2\pi C_0 V_\infty,\tag{5}$$

where V_∞ is the freestream velocity. In Eq. (5) the coefficient A_0 depends only on the angle of attack and the coefficient A_1 depends only on the shape of the mean line. For the particular foils considered here, $1/2(A_0+1/2A_1)=0.04$ was empirically determined. The viscous vortex core size, a_c, is related to the turbulent boundary layer thickness on the pressure side, [1], and has the following expression:

$$a_c=\frac{0.37C_0}{R_e^{0.2}}.\tag{6}$$

The minimum pressure coefficient in the vortex center is then determined by

$$Cp_{\min}=\frac{p_\omega-p_\infty}{0.5\rho V_\infty^2}=-\frac{1}{2\pi^2 V_\infty^2}\left(\frac{\Gamma}{a_c}\right)^2.\tag{7}$$

The flow conditions and parameters for the three cases considered are shown in Table 1.

2.2 Improved Spherical Bubble Dynamics Model (SAP). As in conventional spherical bubble dynamics models we assume that the bubble is too small to modify the "basic" flow field. It however responds dynamically to this field while remaining spherical and its dynamics can be described by the Rayleigh-Plesset equation, [10]. Conventionally, the bubble follows the flow field and sees the liquid pressure, in its absence, at the location of its center as a "far-field" imposed pressure. Here, we modify this equation to account for the presence of a slip velocity between the bubble and the host liquid, and to account for non-uniform pressure fields along the bubble surface. The difference between the liquid velocity $\mathbf{u}$ and the bubble translation velocity $\mathbf{u}_b$, results in an added pressure term similar to that due to a translating sphere in a liquid, and can be shown to be equal to $(\mathbf{u}-\mathbf{u}_b)^2/4$. The detailed derivation can be seen in [11]. Here we account for this term in the modified Rayleigh-Plesset equation as

$$R\ddot{R}+\frac{3}{2}\dot{R}^2=\frac{1}{\rho}\left[p_v+p_{g0}\left(\frac{R_0}{R}\right)^{3k}-P_\infty(t)-\frac{2\gamma}{R}-\frac{4\mu}{4}\dot{R}\right]+\frac{(\mathbf{u}-\mathbf{u}_b)^2}{4},\tag{8}$$

where R is the bubble radius, R_0 *and* p_{g0} are the initial bubble radius and gas pressure, k is the polytropic gas constant, ρ, γ, and μ are the liquid density, surface tension and viscosity, and p_v is the vapor pressure. $P_\infty(t)$ in the classical spherical model is the liquid pressure at the bubble center in its absence. This obviously does not account for pressure variations around the bubble surface, and may lead here to unbounded bubble growth when the pressure in the vortex center is less than the vapor pressure. Previous studies have used this simplification to determine cavitation inception. In the current study we apply a surface averaged pressure (SAP) scheme in which $P_\infty(t)$ is taken to be the average of the outside field pressure over the bubble surface. This enables for a much more realistic description of the bubble behavior, e.g., the bubble does not continuously grow as it is captured by the line vortex. Instead, once the bubble reaches the vortex line axis, it can see an increasing pressure around it as most of its surface moves away from the axis pressure.

The bubble trajectory during capture can be predicted by the following equation of motion, [12]:

$$\frac{d\mathbf{u}_b}{dt}=\frac{3}{\rho}\nabla p+\frac{3}{4}C_D(\mathbf{u}-\mathbf{u}_b)|\mathbf{u}-\mathbf{u}_b|+\frac{3}{R}(\mathbf{u}-\mathbf{u}_b)\dot{R},\tag{9}$$

where the drag coefficient C_D is determined using the empirical equation of Haberman and Morton [13]:

$$C_D=\frac{24}{R_{er}}(1+0.197R_{er}^{0.63}+2.6\times 10^{-4}R_{er}^{1.38}),\tag{10}$$

and the relative velocity Reynolds number is defined by

$$R_{er}=\frac{2R|\mathbf{u}-\mathbf{u}_b|}{\nu}.\tag{11}$$

Equation (9) expresses the balance between drag forces, pressure gradients, and inertia forces due to bubble motion and volume variation. Detailed derivation of (9) from a complete set of motion equation for a spherical particle, [14], can be found among others in [8,15].

The liquid pressure variations at a distance l from the bubble center, resulting from the bubble dynamics is obtained using the expression

$$p=\frac{\rho}{l}[R^2\ddot{R}+2R\dot{R}^2]-\rho\left[\frac{R^4\dot{R}^2}{2l^4}\right].\tag{12}$$

When $l\gg R$ Eq. (12) becomes the expression for the acoustic pressure p_a of Fitzpatrick and Strasberg [16] after introduction of the delayed time t' due to the finite sound speed, c:

$$p_a(t')=\frac{R\rho}{l}[R\ddot{R}(t')+2\dot{R}^2(t')],\quad t'=t-\frac{r-R}{c}.\tag{13}$$

The noise level, SPL, can then be written as:

$$\mathrm{SPL}=20\log\left(\frac{p_a}{p_{\mathrm{ref}}}\right).\tag{14}$$

We use here the conventional value $p_{\mathrm{ref}}=10^{-6}$ N/m².

With the prescribed pressure and velocity flow field given by Eqs. (3) and (4), a Runge-Kutta fourth-order scheme is applied to integrate Eqs. (8) and (9) through time to provide the bubble trajectory and its volume variation during bubble capture by the line vortex. Accuracy in the current numerical scheme is only determined by the time-step size which is found to depend on the initial bubble size. The time-step size should be small enough to resolve the high frequency oscillations as the bubble experiences strong collapse. A time-step size study was conducted to determine needed time step size for each initial nuclei size to obtain less than 0.05% difference in bubble radius and 1% difference in acoustic pressure at their maximum values where the strongest collapse occurs by further reduction by half of the time-step size.

Since this paper was submitted, we have obtained extremely encouraging comparisons (especially relative to the conventional model) between the SAP Rayleigh-Plesset model and a three-dimensional model coupling three-dimensional bubble dynamics and an unsteady Reynolds-averaged Navier-Stokes code, [17].

3 Results and Discussion

3.1 Cavitation Inception Criteria. The precise notion of cavitation inception as a practically observed phenomenon is a matter of discussion. From an engineering viewpoint, cavitation inception is determined through visual or acoustical techniques. Inception is called when the measurement detects events above a predefined threshold. In the laboratory the most commonly used threshold is via visual observation when bubbles "appear." This visual technique can hardly be applied to full-scale tests where an acoustic technique is preferred. In the acoustic technique, the cavitation inception event can be defined either by the sound amplitude level (absolute noise level or relative value over the background noise) and/or by the appearance of some characteristic spikes in the pressure signals. In the current study, both the acoustic and the optical criteria are investigated for determining the cavitation inception. In the following we will also show the importance for numerical simulations of the selection of the bubble dynamics model on the results.

3.2 Cavitation Inception for Line Vortex With Constant Vortex Core. To study scaling effects, the SAP modified Rayleigh-Plesset spherical model was first applied to predict for the three scales described earlier the cavitation inception number, σ_i, for a line vortex with a *nonvarying* vortex core size. Different initial nuclei sizes were also considered to study the effect of the bubble size distribution on cavitation inception. The computations were conducted by releasing the bubbles three core radii away from the vortex axis with an initial nucleus equilibrium condition.

In previous studies, [6–8], the cavitation inception number was determined as the highest cavitation number that leads to an unbounded bubble growth (see Fig. 1). Using this *conventional* model, we found that the predicted cavitation inception numbers for all cases are very close to those given by the simple criterion, $\sigma_i = -Cp_{\min}$. Scaling then follows the relationship given by (2). The results, shown in Table 2, obviously do not explain experimentally measured scaling effects. This way of determining the cavitation inception number stems directly from accepting that the bubble can grow unboundedly once it reaches the vortex center.

Table 2 Cavitation inception number using the classical spherical model approach

R_0	Small Scale	Medium Scale	Large Scale
10 μm	$\sigma_i = 4.467$	$\sigma_i = 13.212$	$\sigma_i = 24.796$
50 μm	$\sigma_i = 4.471$	$\sigma_i = 13.214$	$\sigma_i = 24.796$
100 μm	$\sigma_i = 4.473$	$\sigma_i = 13.214$	$\sigma_i = 24.796$

To account for the fact that the averaged pressure that is imposed on the bubble increases as most of the bubble surface grows away from the vortex axis, the SAP spherical model (averaging the field pressure on the bubble surface) was then applied. Figure 2 shows the bubble radius variation and the acoustic pressure for $R_0 = 50$ μm and $\sigma = 4.471$ in the small-scale case. It is seen that with the modified model both the bubble size and the acoustic pressure reach finite values instead of increasing unboundedly. Therefore, we conducted with the SAP model a series of computations to obtain bubble size and acoustic pressure for different cavitation numbers. Figure 3 shows the maximum bubble size and the maximum SPL measured at 30 cm from the vortex center versus the cavitation number for four different initial nuclei sizes ($R_0 = 10$, 25, 50, and 100 μm) for the medium scale. Similar curves for the small and the large scale can be found in [11].

Based on these curves one can determine the cavitation inception number once an optical or an acoustic threshold criterion is defined. Tables 3 and 4 show the cavitation inception number results obtained for all scales using different illustrative criteria. It is seen that different cavitation inception criteria may lead to significant differences in the resulting cavitation inception numbers. It is also found that the initial nucleus size, R_0, can significantly influence the prediction of the cavitation inception number. For *stringent* (good detection schemes) acoustic or optical criteria (e.g., $\mathrm{SPL}_{\max} > 90$ db or $R_{\max} > 100$ μm), the cavitation inception numbers are definitely not well scaled by Eq. (2) especially for the smaller nuclei. However, for *looser* (high levels needed for detection) criteria (e.g., $\mathrm{SPL}_{\max} > 130$ db or $R_{\max} > 400$ μm), the cavitation inception number is insensitive to the nuclei size and is generally well scaled by Eq. (2).

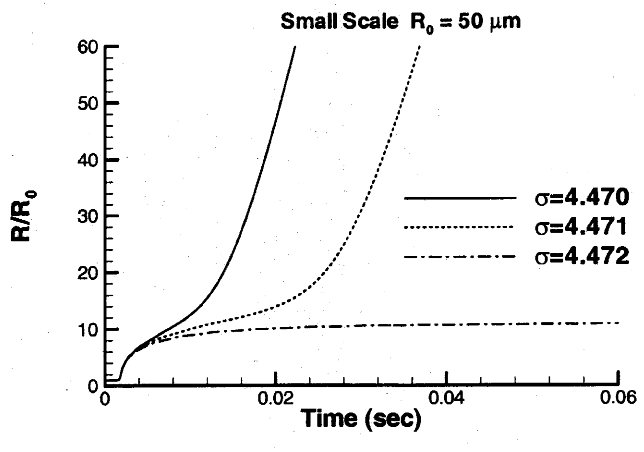

Fig. 1 Bubble radius versus time at different cavitation number obtained by the *classical* Rayleigh-Plesset equation for the small scale with $R_0 = 50$ μm

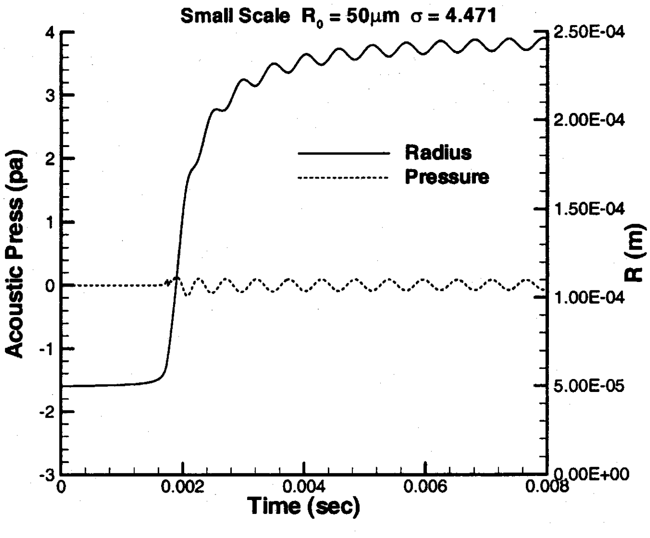

Fig. 2 Bubble radius and acoustic pressure versus time obtained by the modified SAP Rayleigh-Plesset equation for the small scale with $R_0 = 50$ μm at $\sigma = 4.471$

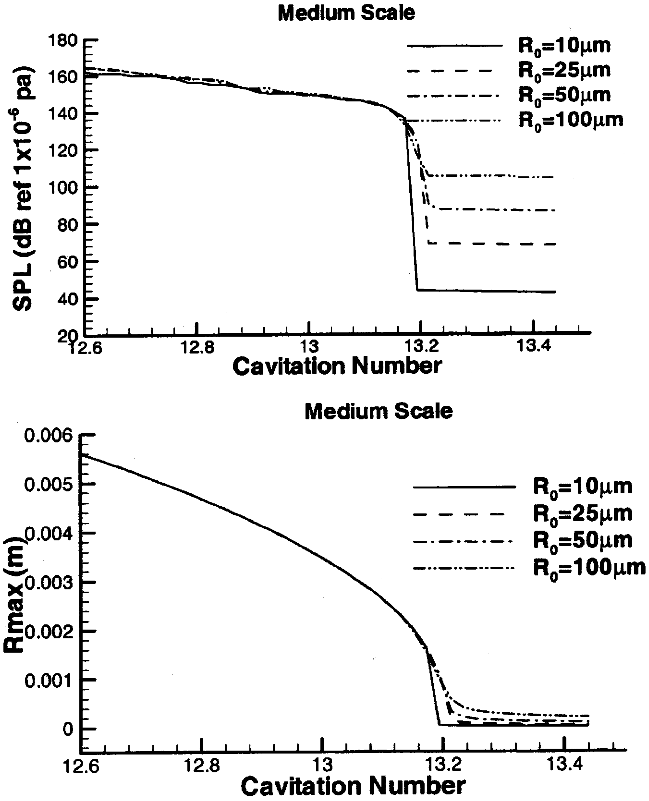

Fig. 3 Maximum SPL and bubble radius versus cavitation number for the medium scale test in the constant vortex core case

Table 3 Cavitation inception number obtained using various illustrative acoustic criteria for defining cavitation inception

Acoustic Criterion		Small Scale	Medium Scale	Large Scale
$-Cp_{\min}$		4.47	13.22	24.80
$\mathrm{SPL}_{\max}$	$R_0=10\ \mu$m	No Inception	$\sigma_i=13.20$	$\sigma_i=24.76$
>90 db	$R_0=25\ \mu$m	$\sigma_i=4.45$	$\sigma_i=13.21$	$\sigma_i=24.77$
	$R_0=50\ \mu$m	$\sigma_i>7$	$\sigma_i=13.21$	$\sigma_i=24.78$
	$R_0=100\ \mu$m	$\sigma_i>9$	$\sigma_i>15$	$\sigma_i>26$
$\mathrm{SPL}_{\max}$	$R_0=10\ \mu$m	No Inception	$\sigma_i=13.17$	$\sigma_i=24.76$
>130 db	$R_0=25\ \mu$m	$\sigma_i=4.36$	$\sigma_i=13.18$	$\sigma_i=24.76$
	$R_0=50\ \mu$m	$\sigma_i=4.36$	$\sigma_i=13.18$	$\sigma_i=24.76$
	$R_0=100\ \mu$m	$\sigma_i=4.37$	$\sigma_i=13.19$	$\sigma_i=24.76$

Table 4 Cavitation inception numbers obtained using various illustrative optical criteria

Optical		Small Scale	Medium Scale	Large Scale
$-Cp_{\min}$		4.47	13.22	24.80
$R_{\max}>$	$R_0=10\ \mu$m	No Inception	$\sigma_i=13.20$	$\sigma_i=24.77$
100 μm	$R_0=25\ \mu$m	$\sigma_i=4.45$	$\sigma_i=13.23$	$\sigma_i=24.82$
	$R_0=50\ \mu$m	$\sigma_i=4.51$	$\sigma_i=13.42$	$\sigma_i>25$
	$R_0=100\ \mu$m	$\sigma_i>5$	$\sigma_i>14$	$\sigma_i>25.5$
$R_{\max}>$	$R_0=10\ \mu$m	No Inception	$\sigma_i=13.19$	$\sigma_i=24.78$
400 μm	$R_0=25\ \mu$m	$\sigma_i=4.41$	$\sigma_i=13.21$	$\sigma_i=24.78$
	$R_0=50\ \mu$m	$\sigma_i=4.41$	$\sigma_i=13.21$	$\sigma_i=24.78$
	$R_0=100\ \mu$m	$\sigma_i=4.42$	$\sigma_i=13.23$	$\sigma_i=24.82$

3.3 Cavitation Inception for Line Vortex With Diffusive Vortex Core

3.3.1 Bubble Dynamics. In the previous section the pressure along the vortex axis was assumed to remain constant. This allowed the bubble to reach some equilibrium status after reaching

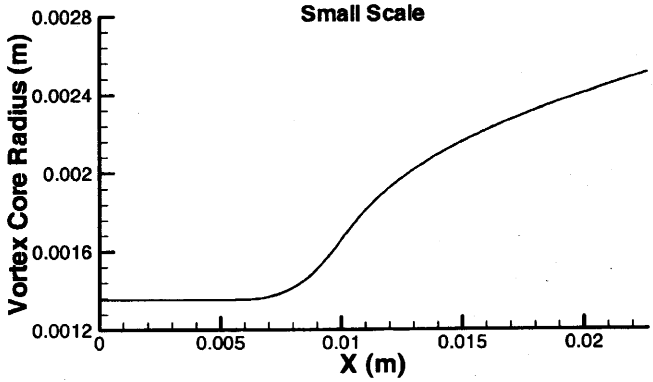

Fig. 4 Diffusion of the vortex core through increase of its radius along the longitudinal direction

the vortex axis. The acoustic emission in this case is mainly from the bubble growth and subsequent oscillations. The bubble collapse, however, is known to generate most of the cavitation noise and occurs after the grown bubble encounters an adverse pressure gradient during its motion. To investigate this effect, a diffusive line vortex was specified by taking into account a vortex core radius increase along the vortex axis as shown in Fig. 4 for the small scale. The *far-field* description of the vortex (i.e., circulation) was kept constant. This is justified by the fact that most of the bubble history occurs over a very short distance from the blade tip. The computations for the diffusive vortex core case were conducted by releasing the bubbles at one half the core radius from the vortex axis with an initial nucleus equilibrium condition. Figure 5 shows the resulting bubble radius variations and the acoustic pressure versus time during the bubble capture for $R_0=50\ \mu$m and $\sigma=4.471$ in the small-scale case.

It is seen that the bubble grows significantly then collapses when it encounters the adverse pressure gradient. Due to the presence of gas in the bubble and to the absence of acoustic energy loss it pursues many successive oscillations. This leads to high-frequency oscillations and stronger acoustic emission than generated during growth. It is interesting to isolate the importance of the slip-velocity pressure term in Eq. (8). The result for neglecting the slip-velocity term is shown in Fig. 6. One can see that much

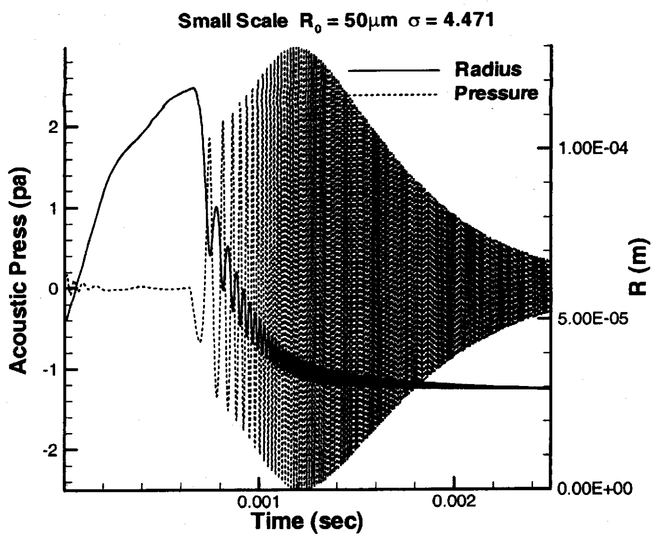

Fig. 5 Bubble radius and resulting acoustic pressure versus time for the small scale with $R_0=50\ \mu$m at $\sigma=4.471$ in a diffusive line vortex

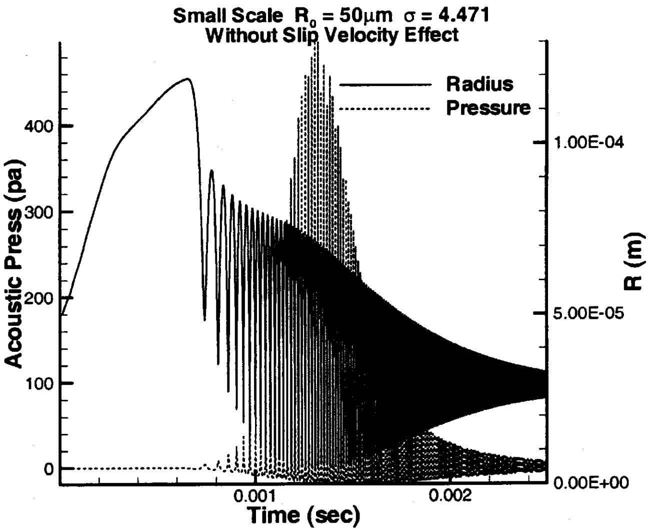

Fig. 6 Bubble radius and resulting acoustic pressure versus time for the small scale with R_0=50 μm at σ=4.471 in a diffusive line vortex when the slip velocity effect is neglected

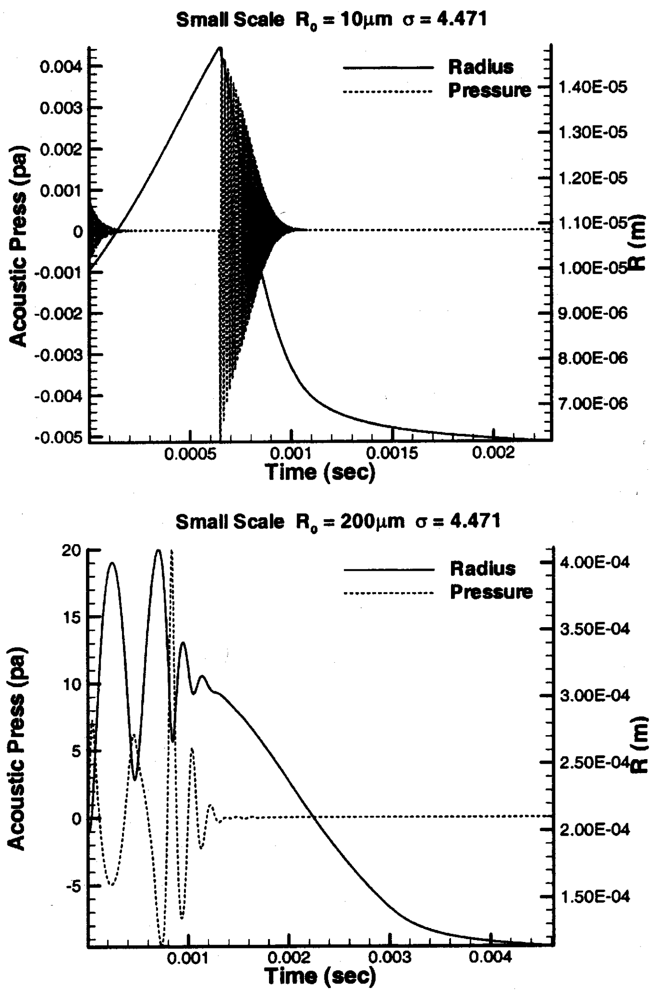

Fig. 7 Bubble radius and resulting acoustic pressure versus time for the small scale with R_0=100 and 200 μm at σ=4.471 in a diffusive line vortex

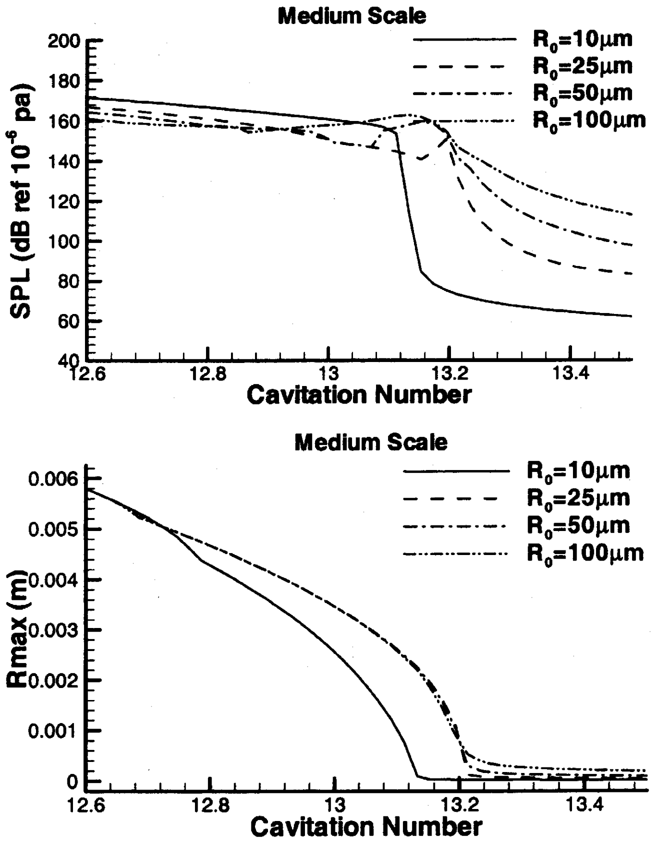

Fig. 8 Maximum SPL and bubble radius versus cavitation number for small and medium scales in the diffusive vortex core case

stronger bubble oscillations occur in this case resulting in extremely high acoustic noise during multiple collapses.

3.3.2 Influence of the Initial Bubble Radius. The influence of nuclei size is studied by releasing bubbles of different initial radii R_0 at the same cavitation number. Figure 7 shows the bubble radius and the acoustic pressure versus time during capture for two extreme sizes R_0= 10 μm and 200 μm at σ=4.471 in the small-scale case. By including the 50 μm case of Fig. 5 one can see different bubble behaviors. The small-sized bubble collapses without strong volume rebound and generates very high frequency but very low amplitude noise, the midsized bubble collapses with strong volume rebound and generates high-frequency and high-amplitude noise. Finally, since the frequency of oscillation of the large-sized bubble is close to that of the encountered pressure field variations, large resonance pressure fluctuations occur. These three different behaviors are also found in the medium and large scales, [11].

3.3.3 Scaling. A series of computations similar to those in the previous section were conducted to obtain the maximum size of the bubble and the maximum acoustic pressure versus the cavitation number. Four initial nuclei sizes (R_0= 10, 25, 50, and 100 μm) were used for all three scales. Figure 8 shows that the maximum bubble size and the maximum noise level SPL measured at 30 cm from the vortex center at the release location versus the cavitation number for the small scale. Similar curves for the medium and large scale can be found in [11]. By comparing Figs. 3 and 8 it is seen that the maximum radius curves are not significantly different from those obtained in the constant core case for the larger initial bubble sizes (R_0=25, 50, and 100 μm). For the smaller initial bubble size (R_0= 10 μm), however, the curves are significantly different from those of constant vortex core because

Table 5 Cavitation inception number obtained using various illustrative acoustic criteria for calling inception

Acoustic Criterion		Small Scale	Medium Scale	Large Scale
$-Cp_{\min}$		4.47	13.22	24.80
$\mathrm{SPL}_{\max}$ >90 db	$R_0=10\ \mu m$	$\sigma_i=4.37$	$\sigma_i=13.15$	$\sigma_i=24.59$
	$R_0=25\ \mu m$	$\sigma_i=4.71$	$\sigma_i=13.38$	$\sigma_i=24.88$
	$R_0=50\ \mu m$	$\sigma_i>6$	$\sigma_i>13.5$	$\sigma_i>25$
	$R_0=100\ \mu m$	$\sigma_i>7$	$\sigma_i>14$	$\sigma_i>25.5$
$\mathrm{SPL}_{\max}$ >130 db	$R_0=10\ \mu m$	No Inception	$\sigma_i=13.13$	$\sigma_i=24.56$
	$R_0=25\ \mu m$	$\sigma_i=4.45$	$\sigma_i=13.22$	$\sigma_i=24.78$
	$R_0=50\ \mu m$	$\sigma_i=4.47$	$\sigma_i=13.25$	$\sigma_i=24.80$
	$R_0=100\ \mu m$	$\sigma_i=4.49$	$\sigma_i=13.32$	$\sigma_i=24.85$

Table 6 Cavitation inception number obtained using various illustrative optical criteria for calling inception

Optical Criterion		Small Scale	Medium Scale	Large Scale
$-Cp_{\min}$		4.47	13.22	24.80
$R_{\max}>$ 100 μm	$R_0=10\ \mu m$	No Inception	$\sigma_i=13.13$	$\sigma_i=24.59$
	$R_0=25\ \mu m$	$\sigma_i=4.45$	$\sigma_i=13.23$	$\sigma_i=24.82$
	$R_0=50\ \mu m$	$\sigma_i=4.49$	$\sigma_i>13.5$	$\sigma_i>25$
	$R_0=100\ \mu m$	$\sigma_i>5.5$	$\sigma_i>14$	$\sigma_i>25.5$
$R_{\max}>$ 400 μm	$R_0=10\ \mu m$	No Inception	$\sigma_i=13.12$	$\sigma_i=24.56$
	$R_0=25\ \mu m$	$\sigma_i=4.39$	$\sigma_i=13.22$	$\sigma_i=24.77$
	$R_0=50\ \mu m$	$\sigma_i=4.41$	$\sigma_i=13.22$	$\sigma_i=24.78$
	$R_0=100\ \mu m$	$\sigma_i=4.41$	$\sigma_i=13.24$	$\sigma_i=24.82$

the bubble with smaller initial size is not always able to enter the vortex center before the vortex core diffuses. To allow the smaller initial bubble size to enter the vortex center before the vortex core diffuses, further decreases of the cavitation number are required. Unlike the maximum radius curves, the maximum SPL curves of diffusive vortex core all differ significantly from those of the constant vortex core, except at high cavitation numbers where the acoustic signal created by the bubble collapse is not stronger than that of growth.

Tables 5 and 6 show the cavitation inception numbers for all the cases considered by choosing the same criteria as in Tables 2 and 3. Unlike in the constant vortex core case where one can select appropriate acoustic and optical criteria such that the cavitation inception number becomes well correlated by Eq. (2), it is very difficult to define such an acoustic or optical criterion for the diffusive vortex core case.

Another way of illustrating the scaling effect due to the nuclei size is to show the cavitation number versus the ratio of the maximum radii obtained at two different scales. This is shown in Fig. 9. To correct for viscous effects the cavitation number is normalized using $\mathrm{Re}^{0.4}$, [18], and the maximum radius using

$$R_m \approx a_c \approx \frac{C_0}{R_e^{0.2}}. \tag{15}$$

Therefore, the ratio between scale 1 and 2 is

$$\frac{R_{m1}}{R_{m2}} = \left(\frac{C_{01}}{C_{02}}\right)\left(\frac{\mathrm{Re}_2}{\mathrm{Re}_1}\right)^{0.2}. \tag{16}$$

The ratio is shown in Fig. 9 for the three groups: middle/small, large/small, and large/middle. It is seen that for each group, the curves of different R_0 are on top of each other for high and low cavitation number but deviate *a lot* right below the cavitation inception point. The normalization factor applied in this study is also expected to merge all the curves of different groups to be equal to one at the low cavitation number. Figure 9, however, shows that the curves of middle/small and large/small approach a value less then one at the low cavitation number. This is because at the low cavitation numbers and in the small scale the bubbles

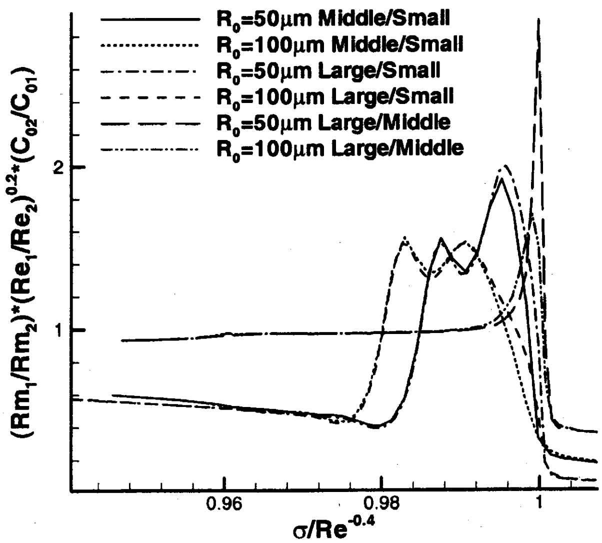

Fig. 9 The normalized curves of the ratio of maximum radius versus cavitation number for three different scale ratio and three different initial bubble size

get trapped at the streamwise location where the vortex diffusion starts to occur while the bubbles are carried downstream for the middle and large scale. An attempt for normalizing the maximum SPL curve has also been tried, but the normalized curves did not merge well due to the difficulty in finding an appropriate characteristic pressure.

3.4 Frequency Analysis. To study further the characteristics of the emitted noise during capture of a bubble in a vortex one can apply a Fourier transformation to the pressure signals. Figure 10 compares the acoustic signals of both constant and diffusive core cases in the frequency domain. Due to the stronger importance of the collapse in the case of a diffusive vortex, one can see that the higher frequencies have much higher amplitudes when compared to the constant vortex core case. The Fourier spectrum for different R_0 and in the diffusive vortex case are shown in Fig. 11 for the small scale. It is found that these curves can be categorized into three major groups according to their shapes.

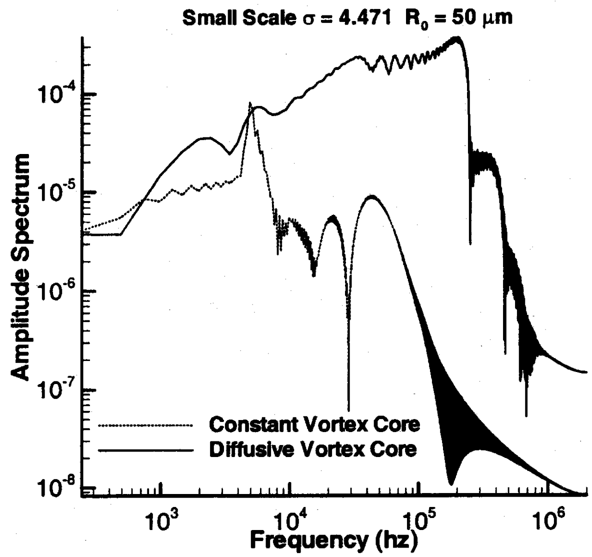

Fig. 10 Comparison of the amplitude spectra of the acoustic pressure generated in a constant and a diffusive vortex core for R_0=50 μm in the small scale

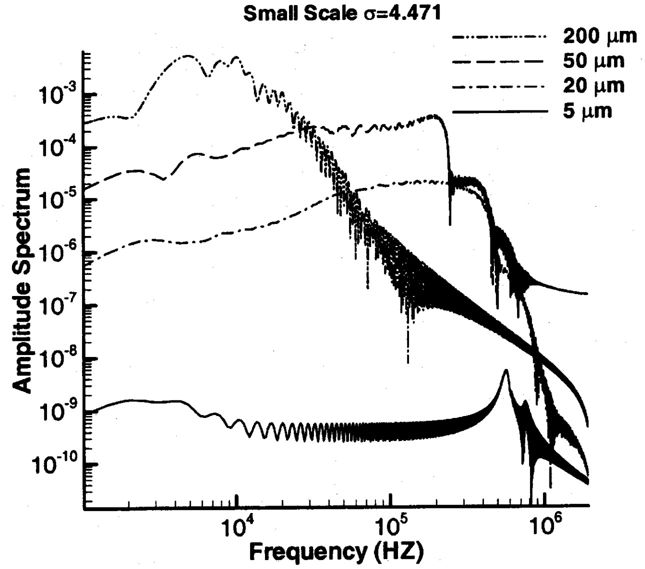

Fig. 11 Amplitude spectrum for various initial nuclei sizes in the small scale

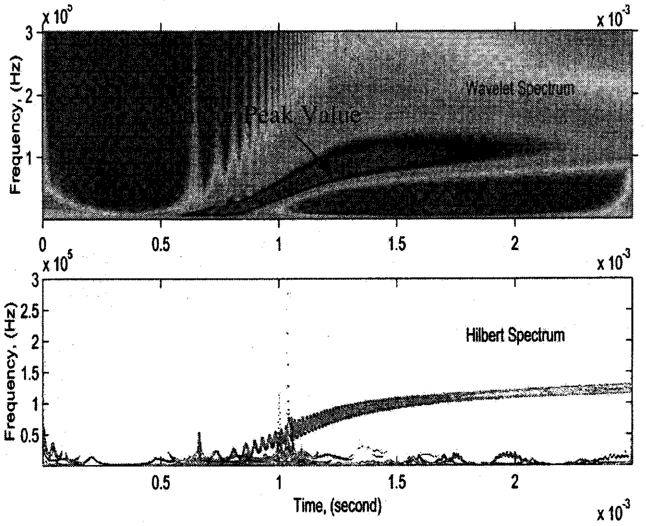

Fig. 13 Wavelet transform and Hilbert transform for R_0 $=50\ \mu$m and $\sigma=4.471$ in the small scale

(a) In the first small bubble size group ($R_0=5\ \mu$m), the curves show two major high frequency peaks, one obtained during initial bubble growth and one during bubble collapse.

(b) In the second middle bubble sizes group ($R_0=20$ and 50 μm), the curves show a rather flat high amplitude region, followed by a power-law decay high-frequency region mainly due to successive bubble collapses.

(c) In the third large bubble size group ($R_0=200\ \mu$m), the curve shows a major amplitude peak at low frequency, which indicates the oscillation frequencies of the bubble growth and collapse, and pressure field variations are very close. This is followed by a gradual classical power-law type decay of the spectrum.

Similar curves are obtained for the other two scales, [11]. It is also found that the bubble sizes for a given group increases as the scale increases.

It is important to know what the peaks in the spectral domain correspond to. To identify these peaks we can estimate the frequency at the location of interest in the acoustic signal generated by a bubble $R_0=50\ \mu$m at $\sigma=4.471$ in the small scale as shown in Fig. 12. One disadvantage of the Fourier transformation is that it does not provide information regarding when in time the various spectral components appear. When the time localization of the spectral components is needed, either a wavelet or a Hilbert transformation, [19], can provide the time-frequency representation. Figure 13 shows the frequency versus time by applying both a wavelet and a Hilbert transformations to the same acoustic signal shown in Fig. 12. Both indicate a high amplitude at the high frequencies (~120 KHz) for a long time after the bubble first collapse. Following the first collapse the frequency of the oscillations increases with each successive collapse. In order to understand this continuous increase in the frequency, we conduct an order of magnitude analysis of the expected bubble oscillations frequency, F, based on the Rayleigh period T,

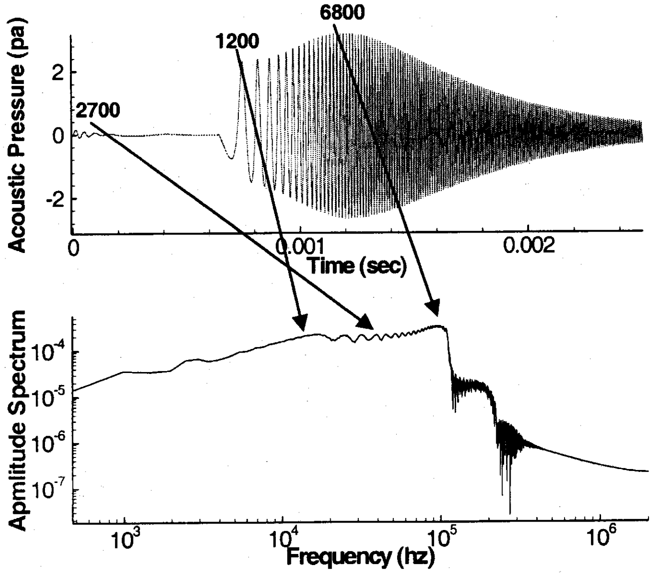

Fig. 12 Correspondence between acoustic signals and the peak frequencies in the Fourier spectrum for $R_0=50\ \mu$m and $\sigma=4.471$ in the small scale

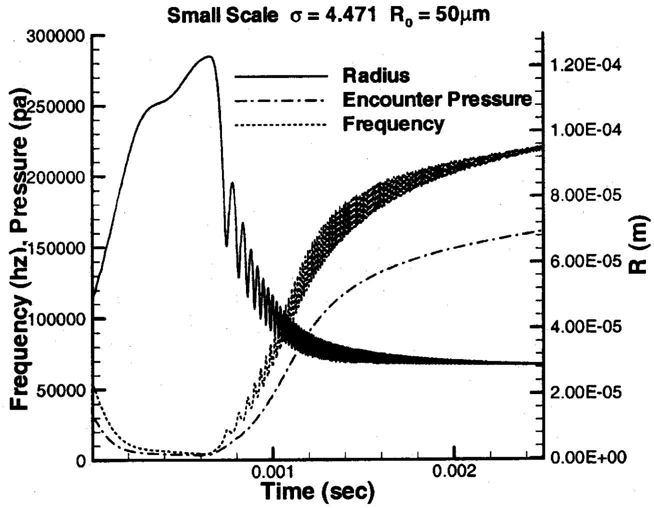

Fig. 14 Bubble radius, encounter pressure and frequency obtained using Eq. (16) versus time for $R_0=50\ \mu$m and $\sigma=4.471$ in the small scale

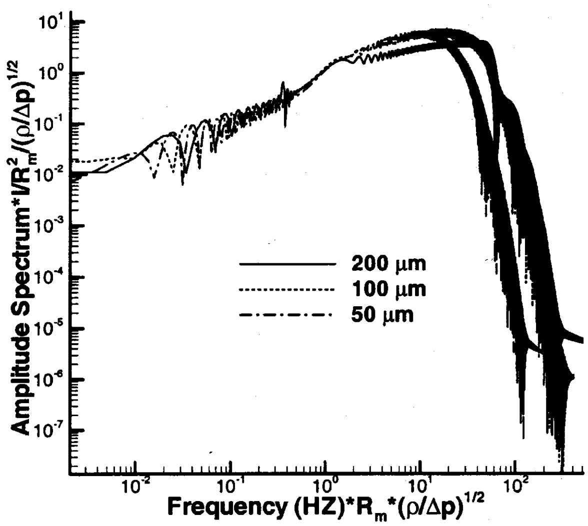

Fig. 15 Normalized amplitude spectra for various initial bubble radii in the large scale

$$F=\frac{1}{2}T^{-1}=\frac{1}{2R}\sqrt{\frac{\Delta p}{\rho}}. \tag{17}$$

Figure 14 shows F versus time computed using the pressure difference $\Delta p = P_\infty(t) - p_v$. This shows the same trend as the Wavelet and Hilbert spectra and appears to give a good approximation of the frequency of the acoustic signals.

From Eq. (17) it appears that the frequency of the first collapse signal is controlled by the maximum radius and pressure gradient at the location where the vortex core starts to diffuse. By appropriately choosing the normalization factor one can obtain a good normalization of the collapse frequency of the second size group discussed earlier. Figure 15 illustrates this for the large scale where more tested nuclei sizes fall in the second group in this scale. The frequencies and amplitudes are normalized by F_m and A:

$$F_m=\frac{1}{R_m}\sqrt{\frac{\Delta P}{\rho}}, \tag{18}$$

$$A=\frac{\Delta P \tau R_m}{l}=\frac{R_m^2}{l}\sqrt{\rho \Delta P}. \tag{19}$$

R_m is the maximum radius, l is the distance to the location where the acoustic signal is computed, and Δp is the difference between the encounter pressure at the first and second bubble collapse.

4 Conclusions

We have used in this study bubble dynamics to predict the cavitation inception in a line vortex flow. We have shown that using the $\sigma = -C_{p\,\min}$ conventional engineering definition of cavitation inception or the classical spherical bubble dynamics model cannot explain experimentally observed nuclei scaling effects. However, the "improved" SAP spherical model shows that the nuclei sizes play an important role in scaling, especially when the water contains only very small bubbles.

We have confirmed that the sources of high-frequency acoustic emission are the initial bubble growth, and more importantly, the subsequent bubble collapse when the bubble reaches the region where the vortex diffuses. The adverse pressure gradient along the vortex core was found to significantly increase both the amplitude and frequency of the acoustic emission during bubble capture by the vortex.

From frequency analysis, it was found that the amplitude spectrum of the acoustical signal can be categorized into three major groups according to their shapes. For the first group, the curves show two major peaks, one from the bubble growth signal and one from the bubble collapse signal. For the second group, the curves show a rather flat high-amplitude region, which is mainly due to successive bubble collapses. For the third group, bubble growth, collapse and pressure field have very similar frequencies and the spectra exhibit only one major peak. By appropriately choosing the normalization factor one can well normalize the first collapse signal of the second group.

Acknowledgments

This work was conducted at DYNAFLOW in execution of a Task Order under the contract N00174-96-C-0034 with the Naval Surface Warfare Center Indian Head Division, Gregory Harris monitor. Funding was provided by the Naval Surface Warfare Center Carderock Division, from the Propulsor Group, Jude Brown. We would like to thank both organizations for their support. We would also like to thank Dr. Young Shen for many useful discussions and suggestions and Dr. Ki-Han Kim for his parallel support.

References

[1] McCormick, B. W., 1962, "On Cavitation Produced by a Vortex Trailing from a Lifting Surface," ASME J. Basic Eng., **84**, pp. 369–379.

[2] Fruman, D. H., Dugue, C., and Cerrutti, P., 1991, "Tip Vortex Roll-Up and Cavitation," *ASME Cavitation and Multiphase Flow Forum*, FED-Vol. 109, ASME, New York, pp. 43–48.

[3] Arndt, R. E., and Dugue, C., 1992, "Recent Advances in Tip Vortex Cavitation Research," *Proc. International Symposium on Propulsors Cavitation*, Hamburg, Germany, pp. 142–149.

[4] Farrell, K. J., and Billet, M. L., 1994, "A Correlation of Leakage Vortex Cavitation in Axial-Flow Pumps," ASME J. Fluids Eng., **116**, pp. 551–557.

[5] Arndt, R. E., and Keller, A. P., 1992, "Water Quality Effects on Cavitation Inception in a Trailing Vortex," ASME J. Fluids Eng., **114**, pp. 430–438.

[6] Latorre, R., 1982, "TVC Noise Envelope—An Approach to Tip Vortex Cavitation Noise Scaling," J. Ship Res., **26**, pp. 65–75.

[7] Ligneul, P., and Latorre, R., 1989, "Study on the Capture and Noise of Spherical Nuclei in the Presence of the Tip Vortex of Hydrofoils and Propellers," Acustica, **68**, pp. 1–14.

[8] Hsiao, C.-T., and Pauley, L. L., 1999, "Study of Tip Vortex Cavitation Inception Using Navier-Stokes Computation and Bubble Dynamics Model," ASME J. Fluids Eng., **121**, pp. 198–204.

[9] Abbott I. H., and Doenhoff, A. E., 1959, *Theory of Wing Sections*, Dover, New York.

[10] Plesset, M. S., 1948, "Dynamics of Cavitation Bubbles," ASME J. Appl. Mech., **16**, pp. 228–231.

[11] Hsiao, C.-T., Chahine, G. L., and Liu, H. L., 2000, "Scaling Effects on Bubble Dynamics in a Tip Vortex Flow: Prediction of Cavitation Inception and Noise," Technical Report 98007-1NSWC, Dynaflow, Inc., Jessup, MD.

[12] Johnson, V. E., and Hsieh, T., 1966, "The Influence of the Trajectories of Gas Nuclei on Cavitation Inception," *6th Symposium on Naval Hydrodynamics*, National Academy Press, Washington, DC, pp. 163–179.

[13] Haberman, W. L., and Morton, R. K., 1953, "An Experimental Investigation of the Drag and Shape of Air Bubbles Rising in Various Liquids," DTMB Report 802.

[14] Maxey, M. R., and Riley, J. J., 1983, "Equation of Motion for a Small Rigid Sphere in a Nonuniform Flow," Phys. Fluids, **26**, pp. 883–889.

[15] Chahine, G. L., 1979, "Etude Locale du Phénomène de Cavitation—Analyse des Facteurs Régissant la Dynamique des Interfaces," doctorat d'etat es-sciences thesis, Université Pierre et Marie Curie, Paris, France.

[16] Fitzpatrick, N., and Strasberg, M., 1958, "Hydrodynamic Sources of Sound," *2nd Symposium on Naval Hydrodynamics*, National Academy Press, Washington, DC, pp. 201–205.

[17] Hsiao, C.-T., and Chahine, G. L., 2002, "Prediction of Vortex Cavitation Inception Using Coupled Spherical and Non-Spherical Models and UnRANS Computations" *24th Symposium on Naval Hydrodynamics*, Fukuyoka, Japan, National Academy Press, Washington, DC.

[18] Shen, Y., Chahine, G., Hsiao, C.-T., and Jessup, S., 2001, "Effects of Model Size and Free Stream Nuclei in Tip Vortex Cavitation Inception Scaling," *4th International Symposium on Cavitation*, Pasadena, CA.

[19] Huang, N. et al., 1998, "The Empirical Mode Decomposition and the Hilbert Spectrum for Nonlinear and Non-Stationary Time Series Analysis," Proc. R. Soc. London, Ser. A, **454**, pp. 903–995.